

ULUSLARARASI 3B YAZICI TEKNOLOJİLERİ
VE DİJİTAL ENDÜSTRİ DERGİSİ

INTERNATIONAL JOURNAL OF 3D PRINTING
TECHNOLOGIES AND DIGITAL INDUSTRY

ISSN:2602-3350 (Online)

URL: https://dergipark.org.tr/ij3dptdi

DEVELOPMENT OF A PHYSICS-INFORMED MELT POOL MODEL FOR POROSITY PREDICTION IN ADDITIVE MANUFACTURING

Yazarlar (Authors): İbrahim Ülke*, Oğuzhan Yılmaz, Mehmet Mollamahmutoğlu

Bu makaleye şu şekilde atıfta bulunabilirsiniz (To cite to this article): *Ulke İ., Yilmaz O., Mollamahmutoglu M., "Development of a Physics-Informed Melt Pool Model for Porosity Prediction in Additive Manufacturing" Int. J. of 3D Printing Tech. Dig. Ind., 9(3): 488-502, (2025).*

DOI: 10.46519/ij3dptdi.1789827

Araştırma Makale/ Research Article

Erişim Linki: (To link to this article): https://dergipark.org.tr/en/pub/ij3dptdi/archive

DEVELOPMENT OF A PHYSICS-INFORMED MELT POOL MODEL FOR POROSITY PREDICTION IN ADDITIVE MANUFACTURING

İbrahim Ülke[a]*, Oğuzhan Yılmaz[a], Mehmet Mollamahmutoğlu[b]

[a]Gazi University, Faculty of Engineering, Department of Mechanical Engineering, TURKIYE
[b]Ankara Yıldırım Beyazıt University, Faculty of Aeronautics and Astronautics, Department of Aerospace Engineering, TURKIYE

* *Corresponding Author: ibrahimulke@gazi.edu.tr*

(**Received:** 23.09.25; **Revised:** 07.10.25; **Accepted:** 15.11.25)

ABSTRACT

Powder Bed Fusion–Laser Beam (PBF-LB) has emerged as a leading additive manufacturing technique for producing complex metallic components; however, its susceptibility to process-induced defects, particularly porosity, continues to limit its widespread application. In this study, a physics-informed computational framework was developed to predict porosity formation in Ti-6Al-4V parts by explicitly resolving transient thermal fields, melt pool dynamics, and layer-wise liquid fractions with temperature-dependent material properties. A dedicated graphical user interface was implemented, providing flexibility in defining the critical processing variables in PBF-LB. Model validation was performed using experimentally reported datasets from the literature. Benchmarking against melt pool geometries demonstrated that the algorithm successfully reproduced the depth and width evolution under different laser powers (100–195 W) and scan speeds (500–750 mm/s). Further comparisons with porosity data revealed strong quantitative consistency: for example, a numerical prediction of 0.19% porosity closely matched Archimedes (0.115%) and μ-CT (0.070%) results, while micrograph-based measurements indicated a higher value (0.204%). Across all investigated specimens, the algorithm reliably reflected experimentally observed porosity trends, including near fully dense conditions (<0.01%). The results demonstrate that the proposed framework provides an efficient and adaptable tool for predicting porosity in PBF-LB prior to fabrication.

Keywords: Porosity Prediction, Thermal Modeling, Ti-6Al-4V Alloy, Additive Manufacturing.

1. INTRODUCTION

Additive Manufacturing (AM) is a production approach in which material is deposited layer by layer, offering the capability to manufacture complex geometries that cannot be realized through traditional techniques. In addition, it offers more design flexibility compared to traditional production methods by using minimum raw materials [1]. Thanks to these features, it is widely used in many sectors such as aviation, automotive, biomedical and energy. However, defects inherent to layer-wise manufacturing processes can significantly impact the structural properties and service performance of the produced components [2]. As a result, the predictability of the internal structure becomes a critical factor in additive manufacturing processes. This is particularly important when alloys such as Ti-6Al-4V are employed, as they are extensively preferred in the aviation and biomedical sectors owing to their superior combination of strength, corrosion resistance, and biocompatibility [3].

Powder Bed Fusion-Laser Beam (PBF-LB) is one of the most widely used types of powder bed melting technologies. The procedure utilises a high-energy laser source to selectively melt metal particles in layers. This facilitates the creation of exceptionally precise components that can be utilised in their original state with minimal or no post-processing. Accurate adjustment of process parameters critically influences the evolution of microstructure and the final quality of fabricated components. Any error or mismatch in these parameters directly affects the energy density transferred to the material. As a result of

the changing energy density, defects can occur in the produced part or on its surface, which directly affect the final product quality [4]. Two of the most common of these defects are porosity and lack of fusion [5]. The main causes of porosity are air bubbles trapped in the powder particles during the raw material production technique [6] and voids formed due to evaporation caused by process parameters [7]. Lack of fusion is mainly due to other reasons such as incomplete melting of some areas of the powder due to inappropriate process parameters and remaining unmelted powder in the shaped parts. Pores directly affect the material density, strength, and overall performance negatively. To popularize the use of PBF-LB technology, time and cost-effective process optimization methods should be developed to eliminate internal structure defects before the process [3]. Many methods have been proposed in the literature for the detection and prevention of porosity. These include non-destructive testing methods, post-processing and machine learning based approaches. Machine learning has become an effective instrument for forecasting faults and enhancing production quality in layered manufacturing processes. Models like Support Vector Machines (SVM) and decision trees are frequently employed to forecast porosity creation and to refine process parameters. Pi et al. showed in their study that porosity prediction can be made in post-production parts using machine learning [8]. In their study where they used the Density Based Spatial Clustering of Noisy Applications (DBSCAN) method. They measured the density of 49 IN718 samples produced experimentally using the Archimedes method and developed four different porosity prediction models. However, the findings indicate that even after removing extreme values from the experimental data, the error rates in the pairwise comparisons between the developed model and the experimental results remain highly variable. Faizan Mohamed et al. used the machine learning method for porosity estimation in the state space in their study where they considered the laser power (50-400 W), scanning speed (750-3000 mm/s) and inter-scan distance (0.0375-0.150 mm) as variables [9]. Unlike the study by Pi et al., they used the Eagar-Tsai thermal model, which is frequently used in powder bed melting processes, to train the reinforcement learning (RL) method. For experimental verification purposes, they made productions with PBF-LB in 12 different parameter combinations using A205 aluminum alloy powders and tested their physically based models. However, when the findings are examined, it is seen that data cleaning is required as in the previous study and the error rates in the estimations vary. Staszewska et al. They combined machine learning classification techniques with regression analysis to analyze the porosity type in PBF-LB [10]. They used AlSi10Mg alloy produced with PBF-LB for training their model. As in all studies using machine learning methods, it is seen that this study includes data preprocessing, manual description, and labeling of pore geometries, then feature selection and data cleaning stages. When the studies in the literature are examined, it is seen that machine learning models generally require large amounts of high-quality data and also need to be trained [11, 12]. However, these methods are often not adaptable to general and are limited to certain data sets [13]. In addition, in real-time quality control applications, machine learning models are generally not fast enough, which has the potential to cause time losses in production processes [14]. In PBF-LB, quality control during production includes monitoring the process using thermal cameras and controlling the parameters as it is carried out [15]. Some experiments using this technique use artificial intelligence to manage heat distribution in the production layer, such as immediate scanning strategy modifications with machine learning [16]. Others, however, are based on more parameter-oriented methods, such as changing the laser power [17] or shifting the laser focus [18].

When the literature is examined, the size and change of the melt pool can be predicted before production starts as an approach different from machine learning with the use of artificial intelligence. It is clearly seen that internal structure analysis can be performed based on process parameters in various melt pool models developed for this purpose [19, 20]. In the PBF-LB method, modeling the melt pool dynamics correctly and optimizing the process parameters require computer-based simulation approaches as an alternative to the experimental trial and error method. In this context, numerical models including physical processes such as thermal conduction, mass transfer and laser absorption are widely used to predict melt pool dimensions

and surface morphology [21]. Numerical models based on direct finite element method such as in the study by Slama et al. are also widely available in the literature aiming at porosity prediction [20]. Models developed based on volumetric heat sources provide a critical tool in understanding the effects of process parameters on the energy distribution within the material. However, such models included partial error rates in the past because they considered parameters such as laser absorptivity and heat conduction coefficient that change with temperature as fixed values. As a result of studies conducted in recent years, the changes of these material-dependent properties with temperature have been better understood and explained [22, 23]. Thanks to these developments, the compatibility with experimental results in melt pool modeling has increased and porosity estimation from melt pool geometry has become more possible. Adapting the temperature-dependent changes of parameters such as heat conduction coefficient or laser absorptivity, which directly affect the melt pool geometry, to mathematical models also brings about an increase in processing load and calculation times. To reduce the calculation time, simulation models that include certain approaches and assumptions to estimate melt pool dimensions are available in the literature. Although attempts have been made to simplify the model by reducing it to a single stitch to reduce processing load in these studies, it is seen that they are insufficient in providing information about porosity in the internal structure directly [24-26].

In this study, an algorithm-based method for porosity estimation in PBF-LB production processes was developed to address a significant gap in the existing literature. Previous numerical models in the literature primarily focused on predicting melt pool geometry or surface morphology as indirect indicators of porosity. In contrast, the proposed model goes beyond melt pool geometry and directly computes porosity within a three-dimensional volume by resolving transient thermal fields, liquid fraction evolution, and layer-wise melt pool overlap. This method allows for voxel-based assessment of interior flaws, offering a physically substantiated estimation of volumetric porosity prior to manufacturing. The developed algorithm incorporates fundamental process variables such as laser power, scan speed, and hatch distance, and it evaluates layer-by-layer porosity distribution in the fabricated part. It can be applied directly prior to production without requiring large datasets, offering faster solutions compared to data-driven machine learning approaches. The proposed methodology was validated using experimental data from the literature, demonstrating its reliability and computational efficiency in predicting porosity formation. This research introduces an innovative, physics-informed methodology that converts melt pool-based thermal modelling into a functional instrument for forecasting volumetric porosity, augmenting quality control, and increasing the industrial relevance of PBF-LB technology.

2. MATERIAL AND METHOD

2.1. Graphical User Interface (GUI) for Process Parameter Control

The user interface presented in Figure 1 enables the definition of initial conditions for the melt pool simulation algorithm developed for the thermal analysis of the PBF-LB process. Physical and numerical inputs required for the simulation are entered by the user and subsequently transferred to the main program as parameters, forming the basis for the mathematical calculations. Laser power and scan speed are the primary parameters influencing the Gaussian-type surface heat profile employed in the heat source model, thereby directly controlling the energy distribution. Beam diameter defines the effective radius of laser interaction in the same function and constrains energy penetration both on the surface and in depth. Substrate and powder temperatures are specified at the beginning of the main function and determine the initial thermal state at the corresponding grid points. Grid size parameter defines the resolution of the three-dimensional computational domain, directly influencing both the spatial resolution of the thermal field and the transmission-based criterion used for calculating the time step. By constraining the time step in accordance with physical stability conditions, this parameter ensures numerical stability throughout the simulation. In turn, the number of powder layers specifies the vertical extent of the computational domain along the Z-direction and is explicitly invoked in functions that track the thermal evolution of the multilayer structure.

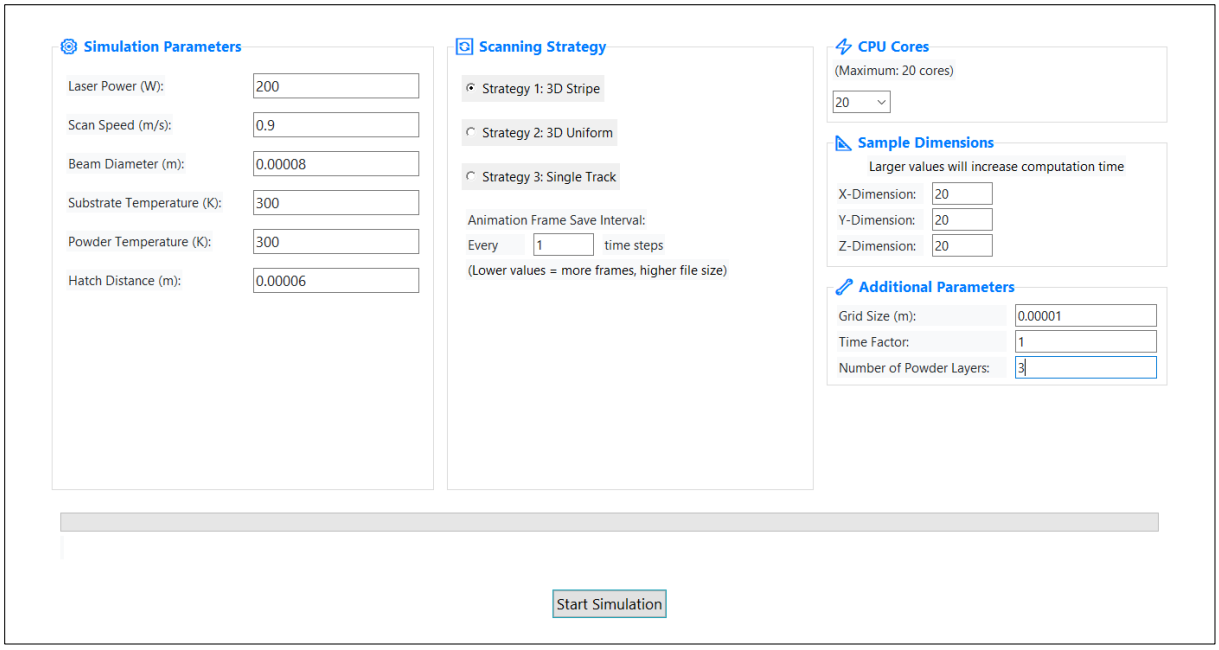


Figure 1. Algorithm graphical user interface.

The number of processor cores specified in the interface determines the parallel computing capacity through the OpenMP library. The sample dimensions section defines the geometry of the part to be simulated. Figure 2 illustrates how process parameters and computational settings are integrated into the algorithm to enable porosity prediction. Inputs provided through the user interface ensure both physical accuracy and computational efficiency. Once all values are entered, the Start Simulation button runs the process, allowing the algorithm to model the thermal effects of laser–material interaction in detail and estimate porosity on a voxel-wise basis.

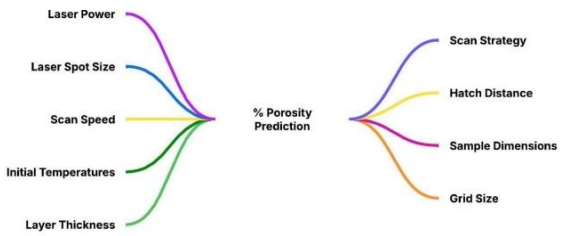


Figure 2. Input parameters affecting % porosity prediction in the algorithm.

2.2. Porosity Prediction Algorithm Flow Chart

A porosity prediction algorithm developed in this study provides a systematic framework for examining the pore structure of Ti-6Al-4V specimens produced by the PBF-LB method and for estimating porosity ratios (Figure 3). Based on the defined process parameters, this algorithm computes transient temperature variations and simulates melt pool dynamics, including the formation and subsequent collapse of the molten region. In addition, layer-wise fill ratios and liquid fractions are incorporated, enabling a more realistic representation of the physical mechanisms governing porosity evolution.

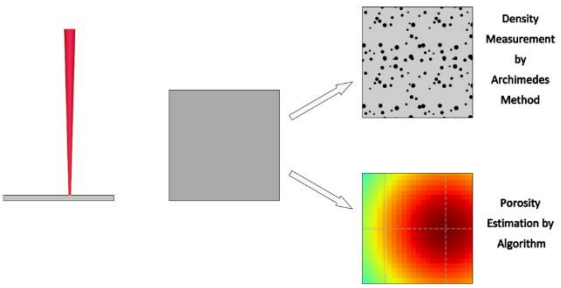


Figure 3. Comparison of experimental and computational approaches

In the algorithm illustrated by the flow chart in Figure 4, the simulation initiates with the solution of the three-dimensional transient temperature field across the computational domain. As the laser beam traverses the surface following the predefined scanning strategy, localized heat input is introduced and balanced by dissipation mechanisms including conduction, convection, and radiation, which are computed for each discretized cell. The resulting thermal field is then coupled with a phase-change formulation that continuously updates the liquid fraction and occupancy rate,

thereby distinguishing liquid, solid, and vapor states within successive layers of the build.

After all layers are processed, the accumulated thermophysical data are analyzed volumetrically to identify pore regions and calculate occupancy values, from which the overall porosity ratio is derived relative to the total sample volume. Within this framework, the algorithm accounts for melt pool dynamics that critically influence defect formation. Material properties of Ti-6Al-4V, including density, thermal conductivity, specific heat capacity, and laser absorptivity, are defined as temperature-dependent constitutive relations embedded in the numerical model, ensuring consistency with the physical process while minimizing user input.

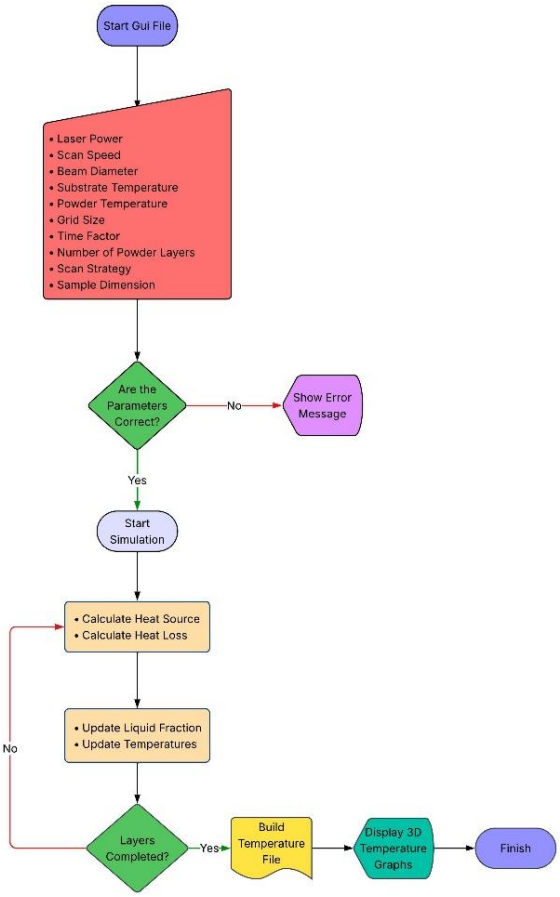


Figure 4. Porosity prediction algorithm flow chart.

2.3. Numerical Implementation and Thermal-to-Porosity Mapping

The developed model predicts porosity formation in PBF-LB processes by resolving the transient thermal fields and relating them to melt pool stability and inter-layer bonding quality. The thermophysical properties of Ti-6Al-4V were defined as temperature-dependent functions, where the specific heat of powder $c_p(T)$ [27], the specific heat of liquid $c_l(T) = 831\ J/kg.K$ [27] and thermal conductivities of solid and liquid phases $k_s(T)$ [27] and $k_l(T)$ [27] govern heat storage and conduction during melting. The effective absorptivity α_{eff} [27] defines the laser–powder interaction efficiency, while the overall effective conductivity $k_{eff}(T)$ captures the contribution of both solid and liquid fractions within each voxel according to the local occupation ratio.

$$c_p(T) = \begin{cases} 483 + 0.215T & T < 1268K \\ 412.7 + 0.1801T & 1268K \le T \le 1923K \end{cases} \quad (1)$$

$$k_s(T) = \begin{cases} 1.25 + 0.015T & T \le 1268K \\ 3.15 + 0.012T & 1268K < T \le 1923K \end{cases} \quad (2)$$

$$k_l(T) = -12.75 + 0.024T \quad (3)$$

$$\alpha_{eff} = \begin{cases} \alpha_p = 0.74 & \text{powder} \\ \alpha_l = 0.26 & \text{liquid} \\ \alpha_l + (\alpha_p - \alpha_l)tanh(22000 \times C) & \text{transition} \end{cases} \quad (4)$$

$$k_{eff}(T) = \begin{cases} k_s(T).\theta & f_{l.max} = 1 \\ (1 - f_{l.max}).k_p(T) + f_{l.max}.\mu(\theta)^2.k_s(T) & other \end{cases} \quad (5)$$

The energy input from the laser source is described by a Gaussian heat flux distribution $Q_{source}(x, y)$, and heat losses through convection and radiation are accounted for by Q_{sink}. Using these boundary conditions, the transient temperature evolution is calculated and then converted into a liquid fraction field $f_{liq}(T)$ for each voxel. The cumulative occupation parameter C describes the local packing density of the powder, influencing both the absorptivity and the heat transfer efficiency.

$$Q_{source}(x, y) \propto \left[erf\left(\frac{\sqrt{2}(x \mp 0.5 - x_0)}{R}\right)\right].\left[erf\left(\frac{\sqrt{2}(y \mp 0.5 - y_0)}{R}\right)\right] \quad (6)$$

$$Q_{sink} = h.A.(T_{surr} - T) + \varepsilon.\sigma.A.(T_{surr}^4 - T^4) \quad (7)$$

$$f_{liq}(T) = \begin{cases} 0 & if\ T < T_s \\ 1 & if\ T > T_l \\ \frac{T - T_s}{T_l - T_s} & if\ T_s \le T \le T_l \end{cases} \quad (8)$$

$$C = \sum_{n=0}^{k-1}(Grid\ size \times Occ(n)) \quad (9)$$

Once the temperature field and phase distribution are resolved, voxels are classified according to their melting and bonding conditions. Voxels with incomplete melting $(f_{L,\max} < f_L^{\text{crit}})$or insufficient track overlap $(O < O^{\text{crit}})$are identified as lack-of-fusion

regions, whereas those with excessive melt-pool depth-to-width ratios ($K_{HD/W} > K^{\text{crit}}$)correspond to keyhole-type voids. The volumetric porosity fraction $\phi$is then defined as the ratio of defective voxels to the total build volume, establishing a direct physics-based linkage between the thermal simulation results and the measurable porosity percentage:

$$\emptyset = \frac{1}{V_{tot}} \sum_i \left(f_{L,max,i} < f_L^{crit} \vee O_i < O^{crit} \vee K_{\frac{HD}{W},i} > K^{crit} \right) \quad (10)$$

This formulation quantitatively connects the melt-pool dynamics with the resulting defect distribution, offering a comprehensive, physics-informed framework capable of predicting porosity prior to fabrication. By directly linking process parameters, transient thermal histories, and melt-pool morphology to the volumetric distribution of pores, the model not only captures the fundamental mechanisms of defect formation but also enables process optimization through predictive control.

3. RESULTS

3.1. Literature-Based Benchmarking of Melt Pool Profiles

The predictive capability of the proposed thermal simulation algorithm was evaluated by benchmarking against experimentally reported melt pool geometries in Ti-6Al-4V fabricated via the PBF-LB process. For this purpose, data from the study of Dilip et al. [28] were considered, focusing on single-track deposits produced at laser powers of 100, 150, and 195 W and scan speeds of 500 and 750 mm/s (Table 1). In accordance with the experimental conditions, a laser spot size of 70 µm and a constant layer thickness of 30 µm were adopted in the simulations. A direct comparison between the experimental melt pool cross-sections reported by Dilip et al. and the numerical predictions obtained from the proposed algorithm is presented in Figure 5. The simulation results reproduced the overall morphological trends observed in the literature, including the transition from shallow, bowl-shaped profiles at lower laser powers to deeper, keyhole-like geometries at higher energy inputs. Specifically, at 100 W and 500 mm/s, the simulated melt pool depth and width were in close agreement with the experimentally reported values, whereas at 195 W and 500 mm/s the model captured the pronounced increase in penetration depth associated with the onset of keyhole formation.

Figure 6 provides a quantitative comparison of melt pool dimensions, thereby reinforcing the consistency between experimental observations and numerical predictions. Both width and depth values predicted by the proposed algorithm exhibited trends that closely followed those measured experimentally across all evaluated parameter sets. Increasing laser power was associated with a systematic enlargement of melt pool width and depth, whereas higher scan speeds led to a reduction in penetration depth; both effects were consistently reproduced by simulations. Table 2 quantitatively summarizes the deviations between experimental and simulated melt pool dimensions. The deviation remains within ±20% for most conditions, while larger discrepancies are observed at high laser powers, consistent with the onset of keyhole instability. Although minor discrepancies were observed in the absolute depth values, particularly under high-energy input conditions, the predicted dimensions remained within the bounds of experimental variability reported in the literature. These results show that the algorithm accurately predicts melt pool dimensions under different process conditions.

Table 1. Laser power and scan speed combinations of test specimen [28].

	S-1	S-2	S-3	S-4	S-5	S-6	S-7	S-8	S-9	S-10	S-11	S-12
Laser Power (W)	100	100	100	100	150	150	150	150	195	195	195	195
Scan Speed (mm/s)	1200	1000	750	500	1200	1000	750	500	1200	1000	750	500

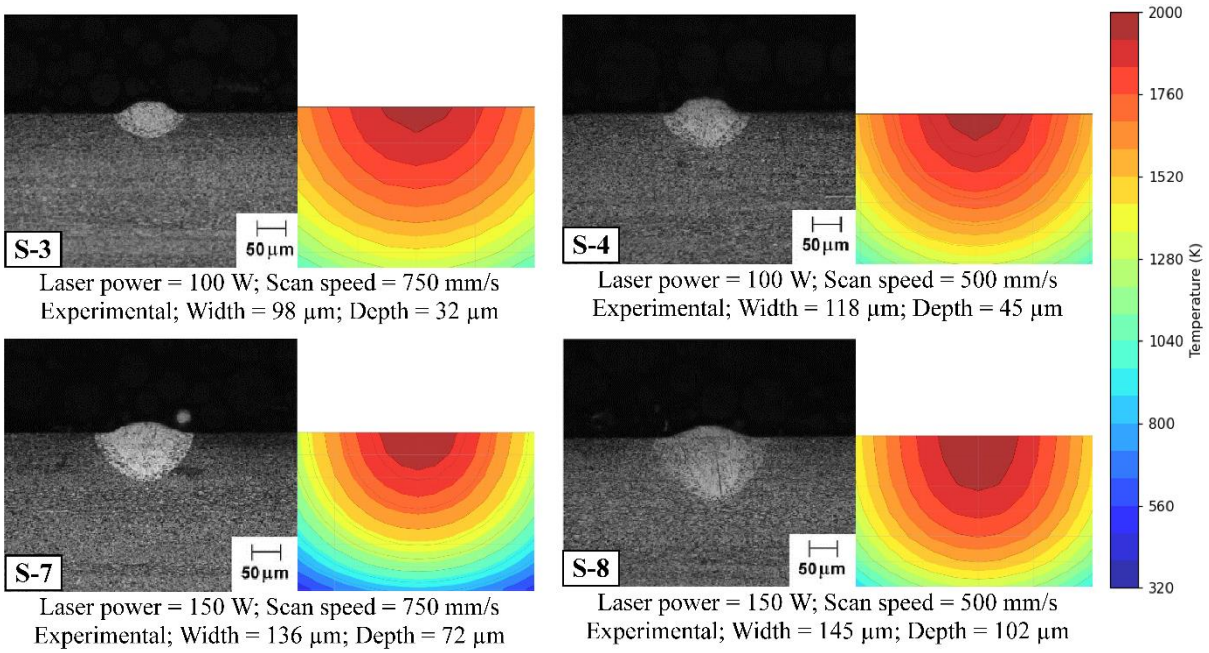


Figure 5. Comparison between experimentally reported melt pool cross-sections [28] and thermal field predictions from the proposed numerical model for Ti-6Al-4V under varying process parameters.

Table 2. Quantitative comparison between experimental and numerical melt pool dimensions [28].

	S1	S2	S3	S4	S5	S6	S7	S8	S9	S10	S11	S12
Depth (Exp., µm)	22	25	32	45	46	54	72	100	64	82	110	178
Depth (Num., µm)	18	22	43	46	38	50	64	89	68	84	96	136
Depth Deviation (%)	-18.2	-12	34.4	2.2	-17.4	-7.4	-11.1	-11	6.3	2.4	-12.7	-23.6
Width (Exp., µm)	72	76	98	119	108	118	136	145	121	130	162	193
Width (Num., µm)	80	83	102	120	112	120	134	137	122	127	138	158
Width Deviation (%)	11.1	9.2	4.1	0.8	3.7	1.7	-1.5	-5.5	0.8	-2.3	-14.8	-18.1

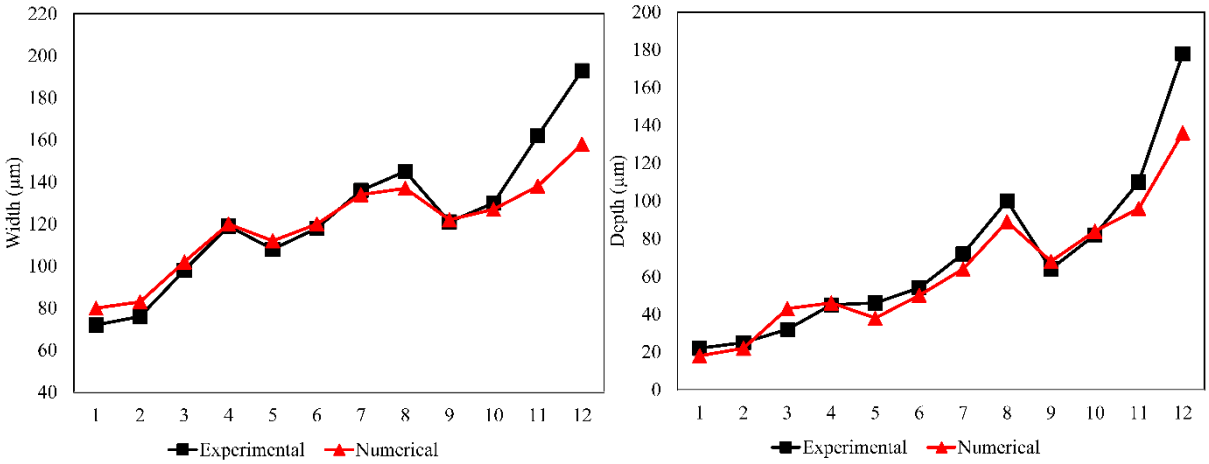
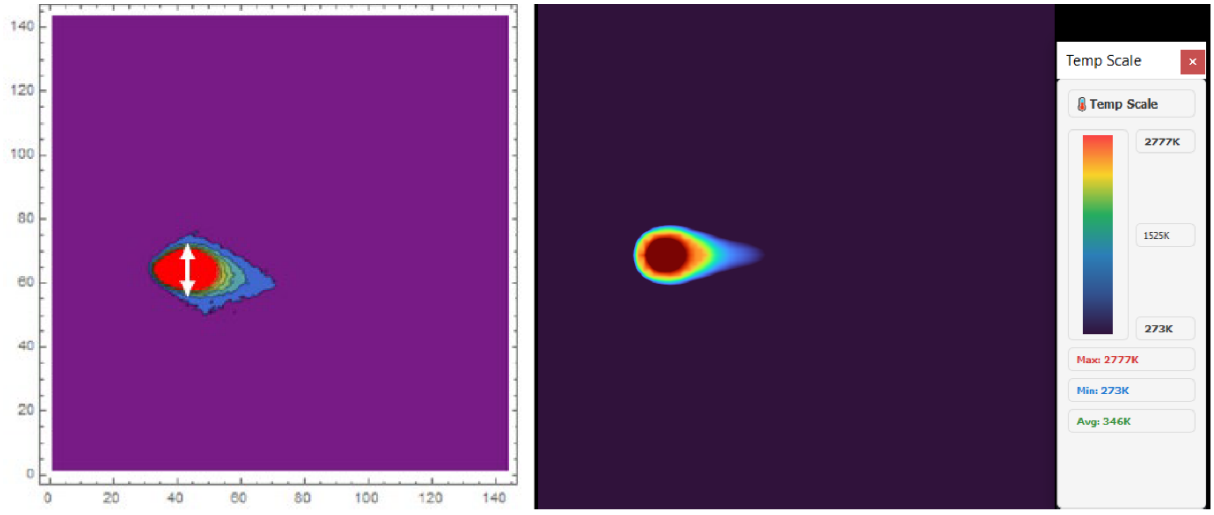


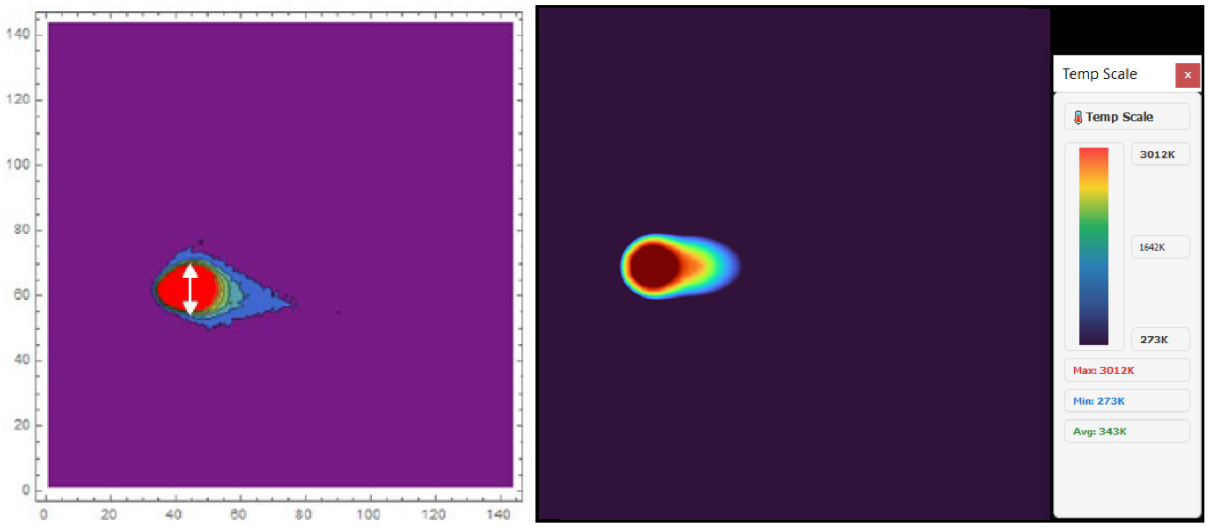
Figure 6. Quantitative evaluation of melt pool dimensions in Ti-6Al-4V under varying laser powers and scan speeds, based on experimental and numerical results.

3.2. Validation of the Proposed Algorithm Using In-situ Melt Pool Imaging Data

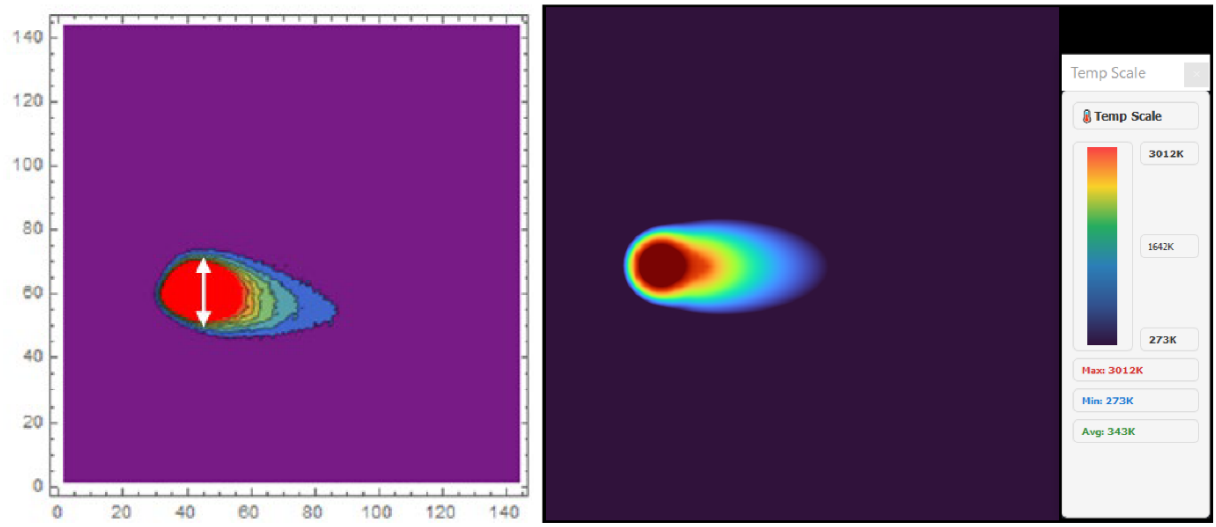
As an additional validation step, the developed numerical model was benchmarked against in-situ imaging data reported in the literature [29]. Zalameda et al. presented near infrared (NIR) measurements of melt pool dimensions on Ti-6Al-4V substrates, calibrated against blackbody sources and validated by optical microscopy. These experimental findings provided a credible benchmark for evaluating the predictive performance of the proposed model.



Case 1 - Laser power: 280 W; Scan speed: 1200 mm/s; Laser spot size: 100 µm



Case 2 - Laser power: 280 W; Scan speed: 850 mm/s; Laser spot size: 100 µm



Case 3 - Laser power: 280 W; Scan speed: 500 mm/s; Laser spot size: 100 µm

Figure 7. Temperature distributions and melt pool profiles of Ti-6Al-4V obtained at different scan speeds. Experimental reference images are shown on the left, while the corresponding results of the proposed numerical model are presented on the right.

In the algorithmic analysis, a computational grid size of 1 μm was employed to achieve high spatial resolution in the thermal field calculations. The initial powder bed and substrate temperatures were set to 300 K, ensuring consistency with typical laboratory conditions. Moreover, the simulations were carried out under a single-track scanning strategy, which allowed for a direct and controlled comparison of melt pool morphology against experimental data.

Figure 7 illustrates the comparison between the reference in-situ measurements (left) and the algorithm predictions (right) for three different scan speeds (1200, 850, and 500 mm/s) at a constant laser power of 280 W and a spot size of 100 μm. The predicted temperature distributions and melt pool geometries showed strong agreement with experimental observations. In particular, the algorithm successfully reproduced the trend of increasing melt pool width and depth as the scan speed decreased, reflecting the higher linear energy input per unit length. These findings demonstrate that the proposed algorithm can realistically replicate melt pool dynamics under varying process parameters. The close correspondence between the simulated fields and NIR-based imaging validates the model's predictive capability and establishes a robust foundation for porosity prediction studies.

3.3. Comparative Analysis of Predicted and Experimental Porosity

Following the validation of melt pool geometries and in-situ thermal signatures, the predictive accuracy of the algorithm was further examined through direct comparison with experimental porosity measurements. While melt pool dimensions and imaging data provide indirect indicators of process stability, porosity quantification offers the most critical measure of part integrity in PBF-LB. Archimedes density analysis was employed to determine the bulk relative density of the fabricated Ti-6Al-4V specimens, whereas high-resolution μ-CT imaging enabled three-dimensional characterization of pore morphology, volume distribution, and spatial clustering. Together, these techniques established a rigorous reference for assessing the model's capability to reproduce experimentally observed defect trends. Within this framework, the numerical predictions were systematically benchmarked against the experimental datasets to evaluate both their quantitative agreement and their consistency in capturing parameter-dependent porosity variations.

In this context, the findings of Promoppatum et al. [30] serve as a valuable reference. Their study systematically compared porosity measurements obtained through optical micrographs and μ-CT in Ti-6Al-4V specimens manufactured under varied scan speeds and hatch rotations. At high volumetric energy densities (≈66.7 J/mm³), both techniques yielded nearly identical porosity values, demonstrating strong consistency. In contrast, pronounced discrepancies were observed in the low-energy regime, where micrograph-based analyses consistently indicated substantially higher porosity levels than those measured by μ-CT. Beyond these quantitative differences, their microstructural observations further revealed isolated and unconnected lack-of-fusion pores, with morphologies strongly dependent on the applied process conditions.

Building upon these insights, the present study adopted the reported experimental observations as a reference for validating the numerical model. The corresponding process parameters, which include a laser diameter of 100 μm, a layer thickness of 30 μm, a hatch distance of 100 μm, and variations in scan speed, are summarized in Table 3.

Table 3. Reported PBF-LB process parameters for Ti-6Al-4V al. [30].

Specimen Number	Laser Power (W)	Scan Speed (mm/s)	Rotation Angle (°)
1	150	750	67
2	150	1500	67
3	150	1875	67
4	150	2500	67

The comparison of porosity obtained from experimental methods is shown in Figure 8, and the overall results are summarized in Table 4. All simulations were performed using an OpenMP-parallelized C solver on a workstation equipped with an Intel Core i9-13900K processor (24 cores: 8 Performance-Cores + 16 Efficient-Cores, 36 MB cache, up to 5.80 GHz) and 32 GB RAM. The computational grid size was fixed at 1 μm, and the time step was 1×10^{-6} s. For the parameter sets corresponding to

Specimens 1–4, each single-track simulation was completed in 2.4 minutes using 8 threads, while each four-layer build simulation required 7.8 minutes under the same configuration.

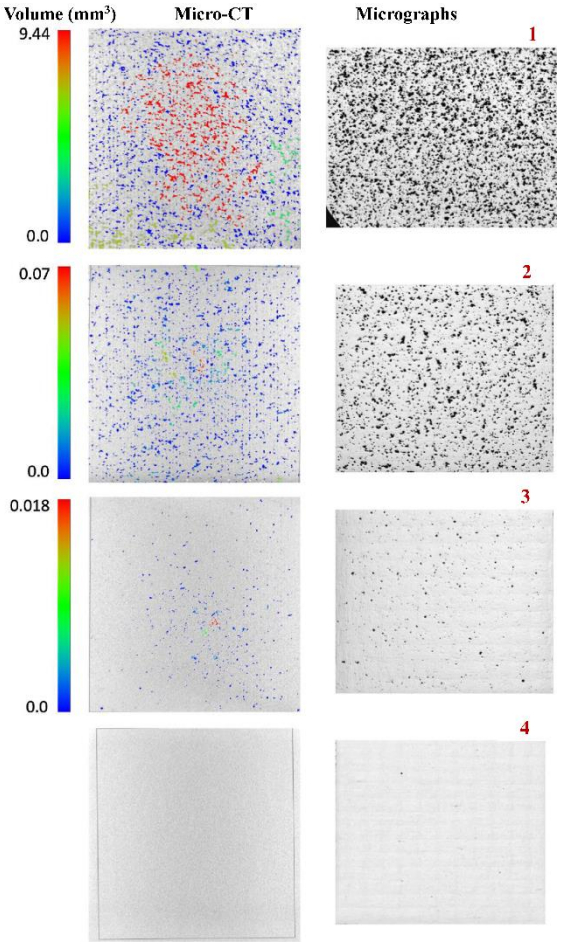


Figure 8. Porosity analysis of the specimens [29].

The μ-CT reconstructions and optical micrographs adapted from Promoppatum et al. [30] provide detailed insights into pore locations and clustering behavior, while the numerical model focuses on estimating overall porosity ratios. Despite this simplification, the predicted porosity levels exhibit close agreement with experimental data. For instance, in Specimen 1 the model predicted 0.32% porosity, which is comparable to Archimedes (0.115%) and μ-CT (0.070%) results, although micrographs indicated a higher fraction (0.204%). Similar levels of consistency are observed for Specimens 2 and 3, and the model successfully reproduced the nearly fully dense condition of Specimen 4. Although the numerical framework demonstrates reliable accuracy in predicting overall porosity levels, it does not yet fully represent the spatial distribution of pores observed in μ-CT analyses. This indicates that, while the algorithm effectively captures defect trends across different process conditions, further refinement is needed to improve its ability to estimate pore positioning.

Table 4. Comparison of experimental and numerical porosity.

Method (%) / Specimen	1	2	3	4
Archimedes	0.115	0.051	0.009	0.002
Micro-CT	0.070	0.048	0.0048	0.00004
Micrographs	0.204	0.086	0.0062	0.0001
Model	0.32	0.14	0.01	0.00

3.4. Cross-Sectional Visualization of Melt Pool Behavior: Experiment and Model Comparison

In the final stage of validation, the proposed numerical framework was performed using the experimental study of Derimow et al. [31], which provides unique in-situ insights into melt pool dynamics during laser melting of Ti-6Al-4V. In this work, high-speed synchrotron X-ray radiography was employed to capture the temporal evolution of melt pool penetration, solidification front movement, and pore formation under controlled process conditions. During the single-track experiments, a laser beam with powers ranging from 200 to 320 W, a constant scan speed of 700 mm/s, and a spot diameter of 80 μm was applied to the prepared specimens. This configuration enabled direct, time-resolved visualization of melt pool behavior, providing a comprehensive dataset against which the numerical predictions of the present study could be critically assessed.

To ensure direct comparison with the synchrotron imaging data, corresponding simulations were performed under identical processing conditions. A voxel size of 1 μm was employed, allowing the model to resolve fine-scale thermal gradients and reproduce melt pool geometries with improved fidelity. Although the localized pore initiation and accumulation evident in the radiographs were not fully captured, the predicted thermal fields exhibited strong consistency with experimentally measured melt pool depth, width, and heat-affected zone extension, thereby underscoring the capability of the framework to reliably represent macroscopic melt pool evolution.

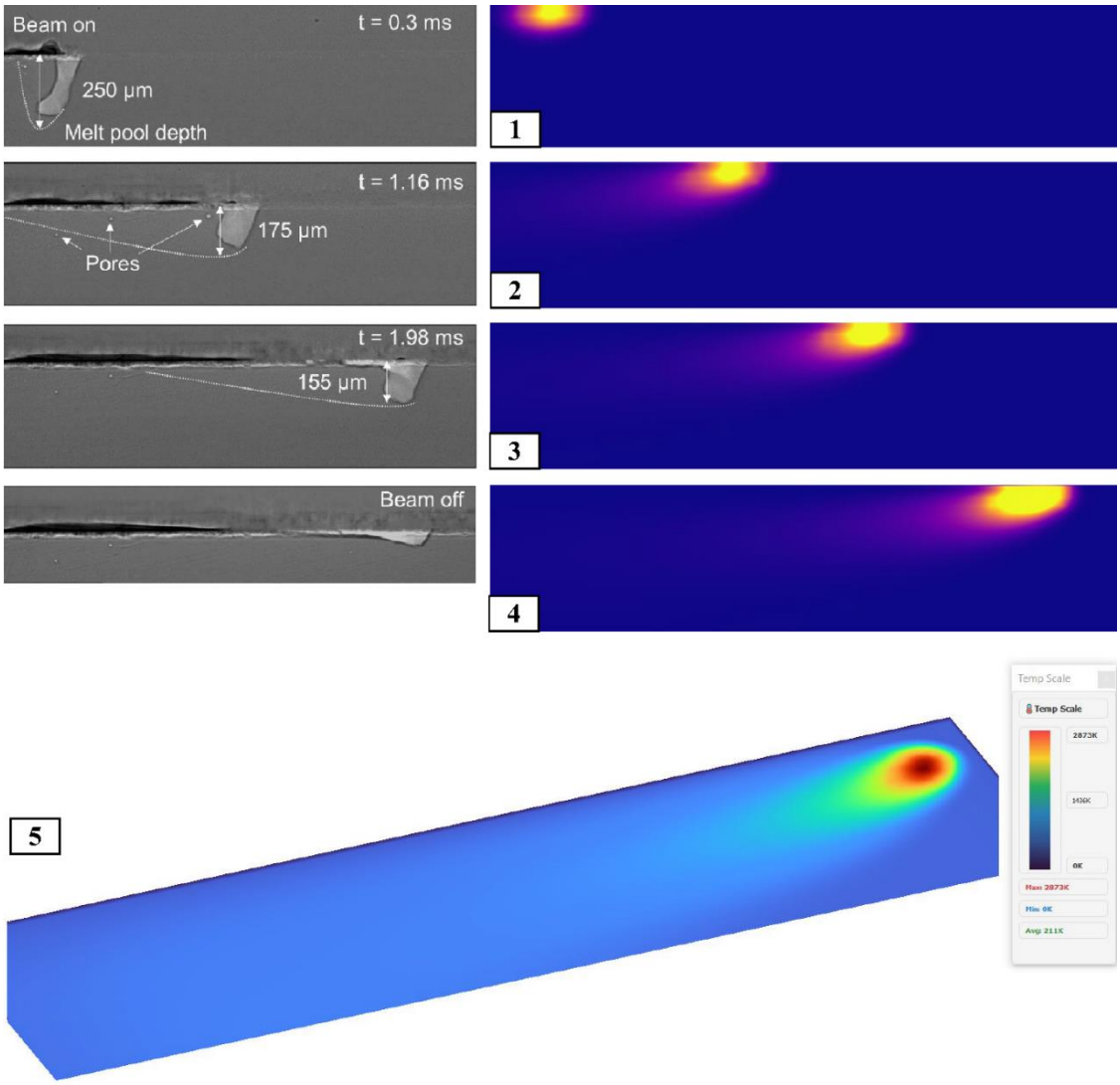


Figure 9. Side-view of melt pool evolution in Ti-6Al-4V: (1–4) experimental cross-sections [31] with corresponding numerical fields, and (5) 3D transient thermal distribution from the model.

4. DISCUSSION

Results obtained in this study indicate that the proposed physics-informed framework provides a reliable and reproducible methodology for predicting melt pool evolution and porosity generation in PBF-LB of Ti-6Al-4V. Comparative analysis with literature-based melt pool profiles revealed strong agreement in reproducing depth and width under moderate laser powers and scan speeds, reinforcing its predictive accuracy in stable regimes. At elevated power levels, however, more significant deviations emerged, highlighting the framework's current inability to fully capture multiphysics effects such as vapor depression and recoil pressure governing keyhole instability.

This was further corroborated by in-situ synchrotron radiography, which provided time-resolved observations of melt pool dynamics. The simulations mirrored the experimental sequence of penetration, progressive shallowing, and final solidification, with the predicted thermal fields aligning closely with experimental trends in melt pool geometry and heat-affected zone extension. Although localized pore initiation evident in the radiographs was not explicitly reproduced, the overall transient melt pool evolution was reliably captured.

From a validation perspective, porosity analysis further highlighted the complexity of experimental validation. As reported by Promoppatum et al. [30], substantial variation was observed between Archimedes, µ-CT, and

micrograph-based porosity values, each technique reflecting different sensitivities to pore morphology, distribution, and sampling volume. Within this variability range, the numerical predictions reproduced the process-dependent porosity trends, particularly under normal and low volumetric energy densities where lack-of-fusion pores dominate, and experimental techniques yield more consistent values. The variability observed among Archimedes, μ-CT, and micrograph-based porosity measurements arises primarily from the dimensional and volumetric sensitivity of each method. The Archimedes technique, while rapid and standardized, provides a bulk estimate of porosity over the entire sample and cannot resolve local pore morphology or connectivity. Optical micrographs, on the other hand, offer detailed resolution but are inherently two-dimensional and strongly dependent on sectioning orientation, which may under- or overestimate pore density in heterogeneous regions.

In contrast, μ-CT analysis enables full three-dimensional reconstruction of the pore network, revealing the volumetric morphology and spatial distribution of defects formed during melting and solidification. Since the proposed model predicts porosity formation based on melt-pool geometry, bonding quality, and volumetric energy distribution, the μ-CT method provides the most physically consistent reference for validation. Accordingly, the porosity values used for direct model comparison in Table 3 were primarily based on μ-CT data, while Archimedes and micrographic results were employed for cross-verification of global trends.

At elevated powers, thermal conductivity and absorptivity relations that depend solely on temperature fail to represent the dynamic coupling between melt flow, vapor recoil, and Marangoni driven convection. These effects alter the local heat transfer pathways and create non-uniform energy absorption, leading to deeper melt pools than those predicted by pure conduction models. Hence, despite incorporating temperature-dependent material properties, the absence of fluid–vapor interactions inherently limit predictive fidelity under keyhole regimes. Similar inconsistencies were reported by Shen et al. [32], where porosity values obtained from optical micrographs were unexpectedly higher than those reported in [30], despite fewer pores being visibly identified. This contrast underscores the methodological uncertainties associated with porosity quantification and highlights the need for caution when interpreting experimental benchmarks across different studies.

The relative importance of process parameters shown in Figure 2 can be interpreted through the governing relations defined in Eqs. (1–10), which collectively determine the transient thermal field and melt-pool morphology. Among these, laser power and scan speed exhibit the strongest and most non-linear effects because they directly control the volumetric energy density and consequently the melt-pool depth-to-width ratio that governs the transition between conduction and keyhole regimes. In Eq. (7), the Gaussian heat-source term $Q_{source}(x, y)$ scales with laser power and determines the spatial heat input, while the cooling losses represented by Q_{sink} remain relatively less sensitive to process variations. As laser power increases, the enhanced heat flux deepens and widens the melt pool, reducing lack-of-fusion defects through improved inter-track bonding. However, beyond a critical threshold, excessive input energy amplifies recoil pressure and vapor depression, producing keyhole-type porosity that the conduction-based model only partially captures.

Conversely, higher scan speeds reduce the exposure time and peak temperature in Eq. (9), lowering the liquid fraction $f_{liq}(T)$ and leading to insufficient melting and isolated pores. Hatch distance and layer thickness influence porosity indirectly through the cumulative occupation parameter C and the effective absorptivity α_{eff} (Eqs. 2 and 10): larger hatch spacing decreases track overlap, while thicker layers increase thermal resistance and reduce absorptivity. These effects collectively explain the parameter-importance hierarchy observed in Figure 2 and confirm that porosity formation in PBF-LB arises from the coupled interplay between local energy density, melt-pool geometry, and solidification kinetics.

Side-view visualization of melt pool dynamics further confirmed the ability of the model to capture the macroscopic thermal envelope and temporal progression of the molten region. The simulations reflected the reduction in

penetration depth and the extension of the thermal tail during beam traversal in close agreement with experimental imaging. Although localized pore accumulation was not resolved, the overall consistency demonstrates that the framework provides a computationally efficient and material-adaptive tool for pre-production porosity assessment in PBF-LB of Ti-6Al-4V, while also emphasizing the necessity of incorporating additional physics to improve predictive fidelity under unstable, high-energy conditions.

5. CONCLUSION

This study developed and validated a physics-informed computational framework for porosity prediction in PBF-LB of Ti-6Al-4V. The main conclusions are as follows:

Framework capability: The model accurately predicts melt pool geometry and porosity evolution under stable processing conditions, confirming its reliability for process–defect assessment.

Porosity predictions: Numerical results remain within the variability of experimental measurements, highlighting consistency despite methodological differences among Archimedes, μ-CT, and optical micrograph techniques.

Practical contribution: The approach provides a computationally efficient and material-adaptive tool that can be applied in pre-production stages to support parameter optimization and quality assurance.

Limitations and outlook: Predictive fidelity decreases at high energy densities, where keyhole instabilities dominate; future work should integrate additional physics (e.g., fluid flow, recoil pressure, vapor depression) and larger datasets to improve resolution of defect mechanisms.

REFERENCES

1. Ero, O., Taherkhani, K., Toyserkani, E., “Optical tomography and machine learning for in-situ defects detection in laser powder bed fusion: A self-organizing map and U-Net based approach”, Additive Manufacturing, Vol. 78, Page 103894, 2023.

2. Wang, S., Ning, J., Zhu, L., Yang, Z., Yan, W., Dun, Y., Xue, P., “Role of porosity defects in metal 3D printing: Formation mechanisms, impacts on properties and mitigation strategies”, Materials Today, Vol. 59, Pages 133-160, 2022.

3. Gui, Y., Aoyagi, K., Bian, H., Chiba, A., “Detection, classification and prediction of internal defects from surface morphology data of metal parts fabricated by powder bed fusion type additive manufacturing using an electron beam”, Additive Manufacturing, Vol. 54, Page 102736, 2022.

4. Guillen, D., Wahlquist, S., Ali, A., “Critical review of LPBF metal print defects detection: Roles of selective sensing technology”, Applied Sciences, Vol. 14, Issue 15, Page 6718, 2024.

5. Gui, Y., Aoyagi, K., Chiba, A., “Development of macro-defect-free PBF-EB-processed Ti–6Al–4V alloys with superior plasticity using PREP-synthesized powder and machine learning-assisted process optimization”, Materials Science and Engineering: A, Vol. 864, Page 144595, 2023.

6. Haiati, S., Dotchev, K., Lowther, M., “Utilizing powder bed fusion additive manufacturing technology to fabricate parts with controlled porosity and permeability characteristics for filtration applications”, International Journal of Precision Engineering and Manufacturing-Green Technology, Vol. 12, Issue 1, Pages 135-149, 2025.

7. Pimenov, D.Y., Berti, L.F., Pintaude, G., Peres, G.X., Chaurasia, Y., Khanna, N., Giasin, K., “Influence of selective laser melting process parameters on the surface integrity of difficult-to-cut alloys: Comprehensive review and future prospects”, The International Journal of Advanced Manufacturing Technology, Vol. 127, Issue 3, Pages 1071-1102, 2023.

8. Pi, Q., Li, R., Han, B., Yang, K., Hu, Y., Shi, Y., Qi, H., “Predicting the porosity of as-built additive manufactured samples based on machine learning method for small datasets”, Optics & Laser Technology, Vol. 177, Page 111203, 2024.

9. Mohamed, A.M.F., Careri, F., Khan, R.H.U., Attallah, M.M., Stella, L., “A novel porosity prediction framework based on reinforcement learning for process parameter optimization in additive manufacturing”, Scripta Materialia, Vol. 255, Page 116377, 2025.

10. Staszewska, A., Patil, D.P., Dixith, A.C., Neamtu, R., Lados, D.A., “A machine learning methodology for porosity classification and process map prediction in laser powder bed fusion”, Progress in Additive Manufacturing, Vol. 9, Issue 6, Pages 1901-1911, 2024.

11. Westphal, E., Seitz, H., "A machine learning method for defect detection and visualization in selective laser sintering based on convolutional neural networks", Additive Manufacturing, Vol. 41, Page 101965, 2021.

12. Mohammed, A.S., Almutahhar, M., Sattar, K., Alhajeri, A., Nazir, A., Ali, U., "Deep learning based porosity prediction for additively manufactured laser powder-bed fusion parts", Journal of Materials Research and Technology, Vol. 27, Pages 7330-7335, 2023.

13. Li, B., Zhang, W., Xuan, F., "Machine-learning prediction of selective laser melting additively manufactured part density by feature-dimension-ascended Bayesian network model for process optimisation", The International Journal of Advanced Manufacturing Technology, Vol. 121, No. 5, Pages 4023-4038, 2022.

14. Kumar, S., Gopi, T., Harikeerthana, N., Gupta, M.K., Gaur, V., Krolczyk, G.M., Wu, C.S., "Machine learning techniques in additive manufacturing: A state of the art review on design, processes and production control", Journal of Intelligent Manufacturing, Vol. 34, Issue 1, Pages 21-55, 2023.

15. Smoqi, Z., Gaikwad, A., Bevans, B., Kobir, M.H., Craig, J., Abul-Haj, A., Peralta, A., Rao, P., "Monitoring and prediction of porosity in laser powder bed fusion using physics-informed meltpool signatures and machine learning", Journal of Materials Processing Technology, Vol. 304, Page 117550, 2022.

16. Park, J.M., Choi, M., Um, J., "Convolutional LSTM based melt-pool prediction from images of laser tool path strategy in laser powder bed fusion for additive manufacturing", The International Journal of Advanced Manufacturing Technology, Vol. 130, Issue 3, Pages 1871-1886, 2024.

17. Carter III, F.M., Porter, C., Kozjek, D., Shimoyoshi, K., Fujishima, M., Irino, N., Cao, J., "Machine learning guided adaptive laser power control in selective laser melting for pore reduction", CIRP Annals, Vol. 73, Issue 1, Pages 149-152, 2024.

18. Zhong, Q., Wei, K., Lu, Z., Yue, X., Ouyang, T., Zeng, X., "High power laser powder bed fusion of Inconel 718 alloy: Effect of laser focus shift on formability, microstructure and mechanical properties", Journal of Materials Processing Technology, Vol. 311, Page 117824, 2023.

19. Yıldız, A.K., Mollamahmutoğlu, M., Yılmaz, O., "Computational evaluation of the effect of build orientation on thermal behavior and in-situ martensite decomposition for laser powder-bed fusion (LPBF) process", Gazi University Journal of Science, Vol. 36, Issue 2, Pages 870-880, 2023.

20. Slama, M.B., Chatti, S., Kolsi, L., "Effect of processing parameters on porosity defects during SLM: A DOE-FEM approach", Welding in the World, Vol. 67, Issue 9, Pages 2201-2213, 2023.

21. Zhang, Z.-D., Shahabad, S.I., Dibia, C.F., Bonakdar, A., Toyserkani, E., "3-Dimensional heat transfer modeling for laser powder bed fusion additive manufacturing using parallel computing and adaptive mesh", Optics & Laser Technology, Vol. 158, Page 108839, 2023.

22. Cook, P.S., Ritchie, D.J., "Determining the laser absorptivity of Ti-6Al-4V during laser powder bed fusion by calibrated melt pool simulation", Optics & Laser Technology, Vol. 162, Page 109247, 2023.

23. Liu, B., Fang, G., Lei, L., Yan, X., "Predicting the porosity defects in selective laser melting (SLM) by molten pool geometry", International Journal of Mechanical Sciences, Vol. 228, Page 107478, 2022.

24. Majeed, M., Vural, M., Raja, S., Shaikh, M.B.N., "Finite element analysis of thermal behavior in maraging steel during SLM process", Optik, Vol. 208, Page 164128, 2020.

25. Ansari Dezfoli, A.R., Lo, Y.-L., Raza, M.M., "Prediction of epitaxial grain growth in single-track laser melting of IN718 using integrated finite element and cellular automaton approach", Materials, Vol. 14, Issue 18, Page 5202, 2021.

26. Domine, A., Verdy, C., Penaud, C., Vitu, L., Fenineche, N., Dembinski, L., "Selective laser melting (SLM) of pure copper using 515-nm green laser: From single track analysis to mechanical and electrical characterization", The International Journal of Advanced Manufacturing Technology, Pages 1-12, 2023.

27. Yildiz, A. K., Mollamahmutoglu, M., Yilmaz, O., "Computational evaluation of temperature-dependent microstructural transformations of Ti6Al4V for laser powder bed fusion process", Journal of Materials Engineering and Performance, Vol. 31, Issue 9, Pages 7191-7203, 2022.

28. Dilip, J.J.S., Zhang, S., Teng, C., Zeng, K., Robinson, C., Pal, D., Stucker, B., "Influence of processing parameters on the evolution of melt pool, porosity, and microstructures in Ti-6Al-4V alloy parts fabricated by selective laser melting", Progress in Additive Manufacturing, Vol. 2, Issue 3, Pages 157-167, 2017.

29. Zalameda, J. N., Hocker, S. J., Tayon, W. A., Fody, J. M., Richter, B. M., "Comparison of in-situ near infrared melt pool imagery to optical microscopy measurements", In Thermosense: Thermal Infrared Applications XLIV, Vol. 12109, Page 1210902, 2022.

30. Promoppatum, P., Srinivasan, R., Quek, S.S., Msolli, S., Shukla, S., Johan, N.S., van der Veen, S., Jhon, M.H., "Quantification and prediction of lack-of-fusion porosity in the high porosity regime during laser powder bed fusion of Ti-6Al-4V", Journal of Materials Processing Technology, Vol. 300, Page 117426, 2022.

31. Derimow, N., Madrigal Camacho, M., Kafka, O.L., Benzing, J.T., Garboczi, E.J., Clark, S.J., Fezzaa, K., Mathaudhu, S., Hrabe, N., "Investigation of melt pool dynamics and solidification microstructures of laser melted Ti-6Al-4V powder using X-ray synchrotron imaging", Journal of Alloys and Metallurgical Systems, Vol. 6, Page 100070, 2024.

32. Shen, T., Zhang, W., Li, B., "Machine learning-enabled predictions of as-built relative density and high-cycle fatigue life of Ti6Al4V alloy additively manufactured by laser powder bed fusion", Materials Today Communications, Vol. 37, Page 107286, 2023.